

# Detectability of Nonlinear Gravitational Wave Memory

Darin C. Mumma<sup>1</sup>

Mentors: Alan J. Weinstein<sup>2</sup>, Colm Talbot<sup>2</sup>, and Alvin K. Y. Li<sup>2</sup>

<sup>1</sup>*Departments of Physics and Philosophy, Grove City College, Grove City, PA 16127, US and*

<sup>2</sup>*LIGO Laboratory, California Institute of Technology, Pasadena, CA 91125, US*

(Dated: July 31, 2020)

Gravitational waves passing through a region of spacetime leave behind a permanent distortion, with strain typically on the order of one tenth the peak strain of the wave—the so-called memory effect. Linear and nonlinear components exist in gravitational wave memory, the latter appearing as a non-oscillatory, cumulative signal. Current gravitational wave detectors have not yet been able to reliably detect and isolate this low-frequency, nonlinear component which skews the numerical inferences of gravitational wave source parameters. Because this effect is cumulative, it is non-negligible, and its non-oscillatory nature distinguishes it from the rest of the waveform, making it detectable, in theory. Though previous studies have quantified and suggested improvements for the detectability of nonlinear memory, more templates and new data are available than ever before. In this project, we apply Bayesian parameter estimation to simulated gravitational waves from compact binary coalescences with memory to determine nonlinear memory detectability.

## I. INTRODUCTION

Although all accelerating masses radiate gravitational waves, compact binary coalescences – binary systems consisting of black holes and/or neutron stars – are especially interesting because they emit the most detectable gravitational wave signals and many of their properties are known [1–3]. The amplitude and phase of a gravitational wave encodes source features such as mass, spin, and location [4]. A typical gravitational wave sourced from a compact binary coalescence is an oscillatory traveling wave with increasing frequency and momentary peak corresponding to the merger phase. As it propagates through spacetime, this waveform distorts surrounding mass arrangements in an oscillating pattern, but afterwards each arrangement returns to its original geometry. However, general relativity predicts that after a gravitational wave passes a truly free-falling arrangement of masses, a memory effect occurs in which a permanent nonzero difference in deformation is observable [5–7].

All gravitational waves produce both linear and nonlinear memory. Linear memory arises from non-oscillating masses and, thus, usually appears only in systems with hyperbolic orbits, neutrino ejection, or gamma-ray bursts [8]. Nonlinear memory arises from the signal contribution of secondary gravitational waves sourced by the initial wave emission. Unlike non-oscillating masses, secondary gravitational wave production occurs in many compact binary coalescences, making nonlinear memory especially prominent. Also, nonlinear memory accumulates over time because it is *hereditary* – depends on the entire past motion of the source. The non-oscillating and cumulative nature of nonlinear memory should, in theory, make it easy to distinguish from the primary component of a gravitational wave signal [9]. In practice this is not the case.

There is one reason why nonlinear memory is, in fact, hard to detect in a gravitational wave signal. As seen in Figure (1), the noise curves for the Livingston and Hanford detectors are minimized between 20–1000-Hz, the typical operating frequency of these detectors. However, nonlinear memory is all below this frequency band, where seismic, control, and quan-

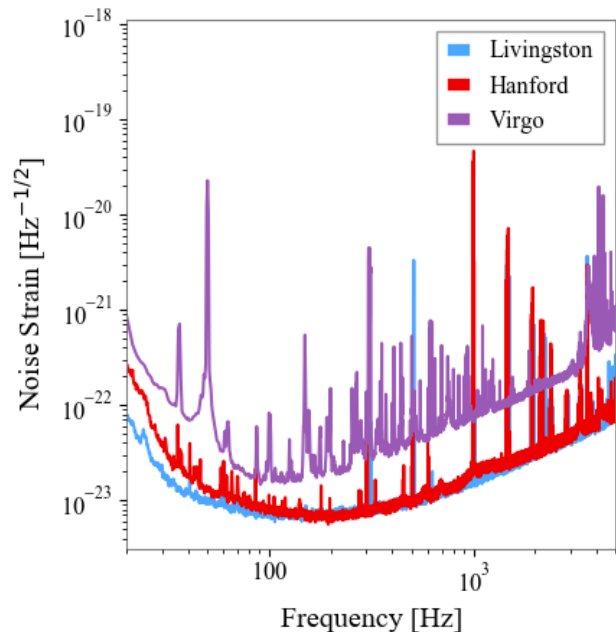


Figure 1. Noise curves beginning at 20 Hz for the LIGO Livingston, LIGO Hanford, and VIRGO detectors during the second observing run. Below 20 Hz, realistic signals cannot be detected because the noise increases many orders of magnitude over the noise shown in this figure.

tum radiation pressure noises dominate. This has long been thought to lower the single-to-noise ratio (SNR) of the memory effect below the resolution of the detectors, rendering it undetectable.

Even in higher frequency bands detector data are very noisy. The primary goal of gravitational wave signal analysis is to distinguish actual signals from this background noise. All phases of compact binary coalescence-sourced waveforms are well modeled using numerical simulations, allowing a template library to be constructed over a broad range of binary component masses and spins. Matched filtering can then be

used to compare these templates with the data and determine the best fit. When nonlinear gravitational wave memory enters the picture, this same process can also be used to determine the detectability of the memory contribution by comparing the memory component in the template with the observed signal in the detectors.

From here, we discuss the theoretical background behind gravitational waves, matched filtering, nonlinear memory, and parameter estimation in Section II. In Section III, we summarize the procedure involved in determining memory detectability. In Section IV, we conclude with a brief discussion of results and future work. Finally, in Section V, we acknowledge the various supporters of this project.

## II. BACKGROUND

### A. Gravitational Wave Theory and Detection

An implication of Einstein's general relativity is that black holes, neutron stars, and other massive objects accelerating in spacetime generate traveling ripples known as gravitational waves [10]. Here we will discuss the speed and polarizations of gravitational waves as well as instruments and methods used to detect them.

#### 1. Speed of gravity

General relativity predicts that gravitational waves propagate at the speed of light,  $c$ , [10], and several measurements have been made to confirm this prediction using astrophysical observations. Most notably, Velten, Jimenez, and Piazza [11] used twenty-five years of orbital decay measurements for the Hulse-Taylor binary, and Abbott *et al* [12] used the difference in arrival time between GW170817 and GRB170817, both sourced from the same binary neutron star merger. The first experimenters were able to constrain gravity's speed to within 1% of  $c$  and the second were able to constrain it to within only  $10^{-13}\%$  of  $c$ .

#### 2. Gravitational wave polarizations and detectors

Another prediction of general relativity is that passing spacetime ripples distort an arrangement of test masses in an oscillatory manner. The frequency and amplitude of the oscillations are related to the angular momentum and mass of the ripple's source, respectively [4]. A Michelson-Morley interferometer may be used to record these variations in spacetime strain: two arms are set perpendicular to one another, and a laser and beamsplitter are arranged at the intersection point as shown in Figure (2). The laser is directed through the beamsplitter, creating two beams which travel along each arm and return after reflecting from mirrors placed at the end of each arm. Both beam paths are aligned to recombine at a photodiode located at the output port of the beamsplitter. Before a gravitational wave passes through, the only phase difference

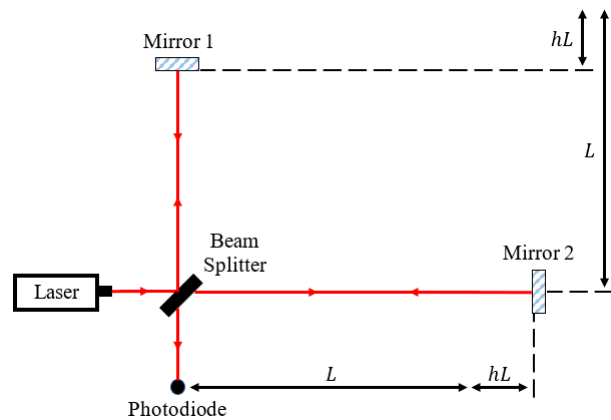


Figure 2. Simplified diagram of a standard LIGO detector. A gravitational wave traveling into the page is incident on the detector, changing each arm length by an amount  $hL$  ( $h$  is gravitational wave strain).

which exists between both beams arises from the difference in arm length, which is carefully adjusted to produce destructive interference at the photodiode.

However, both arm lengths are changed oppositely to one another by a passing gravitational wave, altering the phase difference and, thus, combined intensity of the light incident on the photodiode. This intensity information may be translated to strain information which is given in Equation (1)

$$h_{ij}(t, \mathbf{r}) = \sum_{A=+, \times} e_{ij}^A(\hat{\mathbf{n}}) \int_{-\infty}^{+\infty} h_A(f) e^{-i2\pi f(t - \frac{\hat{\mathbf{n}} \cdot \mathbf{r}}{c})} df, \quad (1)$$

where  $h_{ij}$  is the strain tensor,  $\hat{\mathbf{n}}$  is the wave's propagation direction, and  $t - \frac{\hat{\mathbf{n}} \cdot \mathbf{r}}{c}$  is the retarded time tracking the wave's passage across the detector. In general relativity, the spacetime metric is transverse-traceless gauge invariant, implying that free-falling test masses are at rest in spacetime. Although, the test masses (mirrors) in a given detector are supported by external forces, these are applied at low-frequencies (below 10 – 20-Hz), and are thus negligible at the operating frequencies of ground-based detectors. So, for these detectors, Equation (1) is independent of position  $\mathbf{r}$ , which may thus be set to 0 for a single detector (but will differ for other, non-co-located detectors). Recognizing the resulting integral as an inverse Fourier transform, this yields the expression given in Equation (2)

$$h_{ij}(t) = \sum_{A=+, \times} e_{ij}^A(\hat{\mathbf{n}}) h_A(t), \quad (2)$$

which clearly expresses the total strain as a sum of two polarization states,  $h_+$  (plus) and  $h_\times$  (cross). Both polarization states are transverse to the direction of propagation and are oriented  $45^\circ$  relative to one another as shown in Figure (3). Plus-polarized gravitational waves are a quarter-wave out of phase with cross-polarized gravitational waves, and, generally, incident gravitational waves are a linear combination of

these two polarization states. Thus, gravitational waves may have linear, circular, or elliptical polarizations.

### 3. The Antenna Pattern

Here, we will address the fact that ground-based gravitational wave detectors have variable sensitivity to incident waves sourced from differing sky locations and of differing polarization angles. We will use a reference frame centered on a given detector with its  $z$ -axis normal to the detector's plane and the  $x$ - and  $y$ -axes aligned along the detector's arms. Further, we will use  $\theta$  and  $\phi$  to label the polar and azimuthal angle respectively.

The sensitivity map for a given detector is known as its antenna pattern. This pattern is encoded by the detector response function,  $F_A$ , which may be separated into plus ( $x, y$ -aligned) and cross components and is, as will be shown, a function of  $\theta$  and  $\phi$ . A plus-polarized wave incident at  $\theta = 0$ , oppositely alters the length of both arms, producing maximum detector strain. If this same wave were instead incident at  $\theta = \pi/2$  and  $\phi = 0$ , it would leave one arm unaltered, producing half the detector strain as in the previous case. Finally, if this wave is shifted to  $\phi = \pi/4$ , it alters the  $x$  and  $y$  arms' lengths equally and oppositely, producing zero net strain. With little work, a subtly different pattern is seen with a cross-polarized wave.

Formally, we define  $D^{ij}$ , a constant tensor describing the geometry of the detector, and the detector response function as in Equation (3)

$$\begin{aligned} D^{ij} &= \frac{h(t)}{h_{ij}(t)} \\ F_A(\theta, \phi) &= D^{ij} e_{ij}^A(\theta, \phi) \end{aligned} \quad (3)$$

Combining Equations (2) and (3) yields Equation (4)

$$\begin{aligned} h(t) &= D^{ij} h_{ij}(t) \\ &= D^{ij} \sum_{A=+, \times} e_{ij}^A(\hat{\mathbf{n}}) h_A(t) \\ &= \sum_{A=+, \times} [D^{ij} e_{ij}^A(\hat{\mathbf{n}})] h_A(t) \\ &= F_+ h_+ + F_\times h_\times. \end{aligned} \quad (4)$$

Equation (5) gives  $F_+$  and  $F_\times$  consistent with our observations above

$$\begin{aligned} F_+ &= \frac{1}{2} \cos(2\phi) (\cos^2 \theta + 1) \\ F_\times &= \cos \theta \sin(2\phi). \end{aligned} \quad (5)$$

Plugging these results into Equation (4), we have an expres-

sion which gives noiseless time series data as a function of sky position

$$h(\theta, \phi, t) = \frac{1}{2} h_+ \cos(2\phi) (\cos^2 \theta + 1) + h_\times \cos \theta \sin(2\phi). \quad (6)$$

### 4. Signal types

There are multiple, known gravitational wave types including continuous, stochastic, burst, and compact binary coalescence gravitational waves [13–15]. Continuous gravitational waves are radiated by spinning neutron stars and thus maintain constant frequency and amplitude. Stochastic gravitational waves likely come from especially distant sources and thus arrive from all directions, at all frequencies, and at all times. Burst gravitational waves have waveforms that are difficult to predict in advance but nevertheless exist as short duration pulses. Relevant to this paper, compact binary coalescence gravitational waves are sourced from inspiraling compact objects, such as binary black holes and/or neutron stars, and thus vary in frequency and amplitude over time. Compact binary coalescences consist of three phases, including an inspiral, merger, and ringdown as shown in Figure (4). In the inspiraling stage, the separation distance and orbital period of the binary components decay due to radiated energy in the form of gravitational waves. This portion of the signal increases in frequency and amplitude as the merger approaches. In the merger phase, the signal's amplitude briefly peaks as the binary components combine. In the ringdown stage, the resulting merged black hole (or heavy neutron star) stabilizes, producing a signal with exponentially decreasing amplitude. Among these four types of gravitational waves, compact binary coalescence gravitational waves have the most well-modeled waveforms and are the only gravitational wave sources detected by LIGO-VIRGO thus far [1–3].

### 5. Detection methods

Increased detector sensitivity is achieved by equally extending both beam paths through the careful arrangement of mirrors which allow multiple reflections to take place before the beams are recombined. As a result, typical detector sensitivity allows for measurements of strain on the order of  $10^{-23}$ . Even if a given gravitational wave signal is louder than this, background noise, both local and non-local, can mask or even mimic the signal [16]. Random noise, such as quantum and thermal noise, are often due to local causes and is thus uncorrelated among an array of distant detectors, whereas a passing gravitational wave is incident on every point of the earth nearly simultaneously. So, using the *coincidence criterion*, comparison of data among multiple detectors may be used to distinguish real signals from random signals. The coincidence criterion may also be used to identify non-local noise such as earthquakes and other seismic waves (e.g. those caused by ocean waves colliding with the continental plates). During

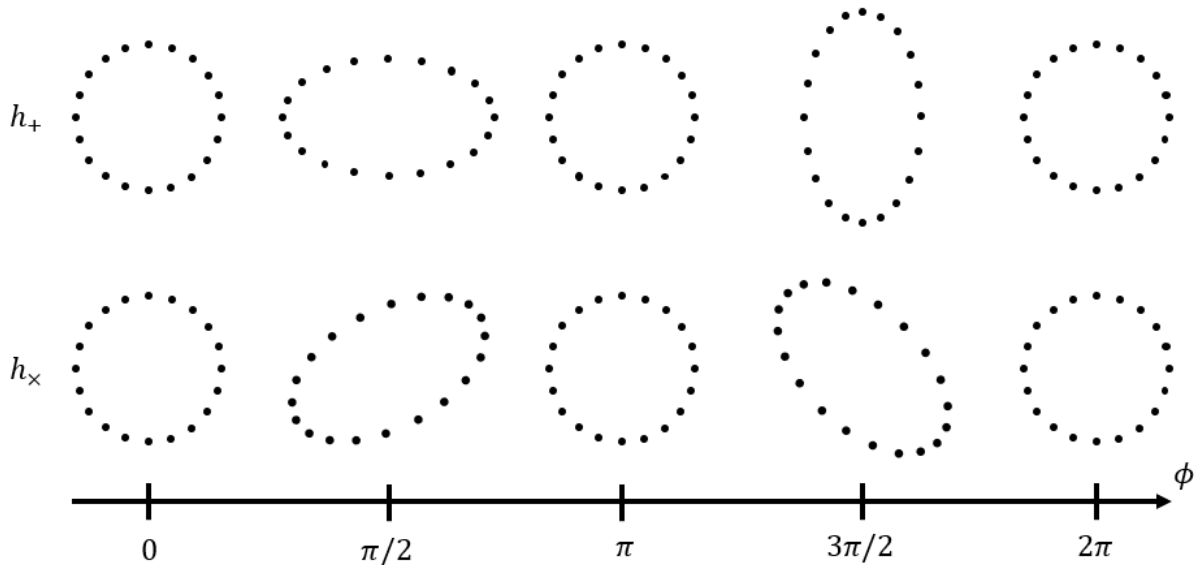


Figure 3. Linear polarizations of a gravitational wave illustrated over a complete phase cycle. Each dot represents a distinct test mass and the wave propagates into the plane of the paper.

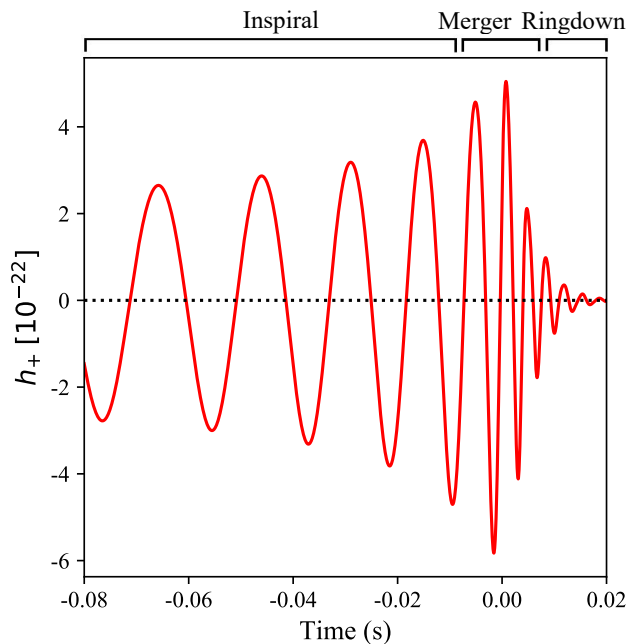


Figure 4. Compact binary coalescence gravitational-wave strain amplitude that shows the full bandwidth of a typical waveform. The inset labels indicate the inspiral, merger, and ringdown phases of two coalescing black holes.

periods of low seismic activity, gravitational wave candidates may still be trusted; however, during periods of intense seismic activity, any gravitational wave candidate is often untrustworthy and may be rejected outright. Methods to reduce noise and increase detector sensitivity are shown in Figure (5). Identifying gravitational waves is further improved by comparing

data to numerical templates constructed according to general relativity. This process, known as matched filtering, is explained in the next section.

## B. Matched Filtering

Matched filtering plays an important role in identifying gravitational waves and determining memory detectability through parameter estimation. Here we will start by describing matched filtering without memory and then include memory afterwards.

The ability to extract a signal from background noise is given by the SNR,  $\rho$ , which is typically between 5 and 25 in an Advanced LIGO detector for realistic, detectable compact binary coalescences, and matched filtering is a process by which it may be computed [18]. In matched filtering, gravitational wave templates are cross-correlated with observed data in the frequency domain by sliding template waveforms along the data until a maximum correlation value is reached. This requires us to introduce a filter kernel,  $\tilde{K}(f)$ , which is related to the template in some way to be determined as described below.

First, the correlation value,  $\hat{s}$ , is related to the strength of the signal,  $\langle S \rangle$ , according to Equation (7)

$$\begin{aligned} \langle S \rangle &= \langle \hat{s} \rangle = \int \langle \tilde{s}(f) \tilde{K}(f) \rangle df \\ &= \int \tilde{h}(f) \tilde{K}^*(f) df, \end{aligned} \quad (7)$$

where  $\tilde{s}(f) = \tilde{h}(f) + \tilde{n}(f)$  is the data in the frequency domain,  $\tilde{h}(f)$  is the signal's waveform,  $\tilde{n}(f)$  is the background noise,

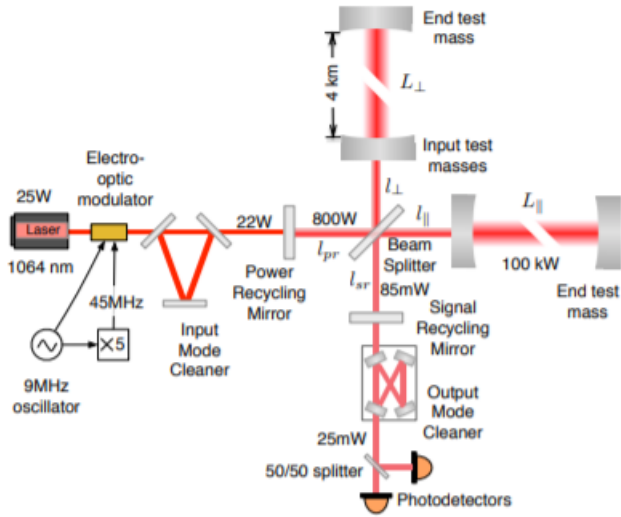


Figure 5. More detailed diagram of an Advanced LIGO detector. The annotations show the optical power in use during the first LIGO observing run. The Nd:YAG laser, with wavelength  $\lambda = 1064\text{-nm}$ , is capable of producing up to 120-W, but only 22-W were used. A suspended, triangular Fabry-Perot cavity serves as an input mode cleaner to clean up the spatial profile of the laser beam, suppress input beam jitter, clean polarization, and help stabilize the laser frequency. The Michelson interferometer is enhanced by two 4-km-long resonant arm cavities, which increase the optical power in the arms by roughly a factor of 270. Since the Michelson interferometer is operated near complete destructive interference, all but a small fraction of the light is directed back towards the laser. The power recycling mirror resonates this light again to increase the power incident on the beamsplitter by a factor of nearly 40, improving the quantum Poisson noise sensing limit and filtering laser noises. An output mode cleaner is present at the antisymmetric port to reject unwanted light components before the signal is detected by the main photodetectors. Retrieved from Martynov *et al* [17].

and  $\tilde{K}(f)$  is the filter function. The second line is obtained by assuming  $\tilde{n}(f)$  is random, making  $\langle \tilde{n}(f)\tilde{K}(f) \rangle = 0$ .

Second, let the one-sided power spectral density of the data's noise,  $S_n(f)$ , be defined as  $\langle |\tilde{n}(f)|^2 \rangle$ . Then, if no signal is present,  $\tilde{h}(f) = 0$  and the root mean square of the noise,  $N$ , is given by

$$\begin{aligned}
 N &= \sqrt{\langle \hat{s}^2 \rangle - \langle \hat{s} \rangle^2} \Big|_{\tilde{h}=0} \\
 &= \sqrt{\int \langle \hat{s}^2 \rangle df} \\
 &= \sqrt{\int \langle \tilde{n}(f)\tilde{n}(f') \rangle \tilde{K}(f)\tilde{K}(f') df df'} \quad (8) \\
 &= \sqrt{\frac{1}{2} \int S_n(f) |\tilde{K}(f)|^2 df}.
 \end{aligned}$$

Thus,  $\rho = \frac{\langle S \rangle}{N}$  may be written as

$$\rho = \frac{\int \tilde{h}(f)\tilde{K}^*(f) df}{\sqrt{\frac{1}{2} \int S_n(f) |\tilde{K}(f)|^2 df}}, \quad (9)$$

or, defining the inner product between  $\tilde{x}$  and  $\tilde{y}$  as

$$\langle \tilde{x}, \tilde{y} \rangle = \mathbb{R} \left( \int \frac{\tilde{x}(f)\tilde{y}^*(f)}{\frac{1}{2}S_n(f)} df \right), \quad (10)$$

$\rho$  can be simplified, yielding

$$\rho = \frac{\langle \frac{1}{2}S_n\tilde{K}, \tilde{h} \rangle}{\sqrt{\langle \tilde{h}, \tilde{h} \rangle}}. \quad (11)$$

It is readily seen that Equation (11) is maximized when  $S_n\tilde{K} \propto \tilde{h}$ , or, equivalently, when

$$\tilde{K}(f) \propto \frac{\tilde{h}(f)}{S_n(f)}. \quad (12)$$

If we redefine  $\rho$  as the time series  $S(t)/N$  by applying a fast Fourier transform to the combination of Equations (7) and (12), we have

$$\rho(t) = \frac{1}{N} \int \frac{\tilde{s}(f)}{S_n(f)} \tilde{h}(f) e^{i2\pi ft} df, \quad (13)$$

from which we can see that  $\tilde{K}(f)$  has the effect of suppressing frequencies where the Gaussian noise is high, allowing signal frequencies to be heard more easily.

Whitening is a process in which a spectrum is divided by  $\sqrt{S_n(f)}$ . With this in mind, Equation (13) tells us that we must first whiten the data and our selected template, only afterward cross-correlating the two. The result is interpreted as an SNR time series which only achieves large values if a signal is present and agrees closely with the template.

Matched filtering can be performed for a network of detectors with the network SNR given in Equation (14)

$$\rho_{net} = \sqrt{\sum_i \rho_i^2}, \quad (14)$$

where  $i$  runs over each detector and  $\rho_{net}$  is referred to as the network SNR. Typically, signals must have  $\rho_{net} \gtrsim 10$  to be detected, but both signals and glitches can satisfy this requirement, introducing the significant possibility of false detection. We can drastically reduce the likelihood of false detection by requiring each  $\rho_i$  to be above a certain threshold within 11-ms between the Hanford and Livingston detectors or 25-ms between the Hanford and VIRGO detectors; this is the coincidence criterion mentioned above.

Matched filtering can also be used with templates having a memory contribution, allowing the detectability of memory to be calculated. If the output of the matched filter using a template containing memory yields a significantly higher SNR from the data than the output using a template without memory, the memory is detectable. The mathematical details involve parameter estimation and computation of a Bayes' factor, which will be explained after a discussion of nonlinear memory.

### C. Nonlinear Memory Theory

The nonlinear (Christodoulou) gravitational wave memory is a permanent strain in spacetime due to the passage of gravitational waves [8, 9]. According to general relativity, a post-Newtonian expansion exists in which nonlinear memory is described by terms which immediately follow the primary waveform and linear memory. However, far from being negligible, these terms accumulate memory over the duration of the signal, increasing most rapidly during the merger as seen in Figure (6). These increasing terms arise from the signal contribution of secondary gravitational waves sourced by the primary waveform, and can thus be viewed as linear memory from waves which began from an arbitrary point in spacetime. Nonlinear memory is shown in Figure (7) for a plus polarized signal. The non-linear component is readily seen to be substantial.

The strength of nonlinear memory depends on incident angle in much the same way as the primary waveform (see Equation (6)) and, as just mentioned, changes monotonically over time. It is clear, then, that nonlinear memory has an angular and temporal dependence which vary independent of one another, suggesting separation of variables. Indeed, through an application of separation of variables and projection of the linear polarizations of the waveform onto the spherical harmonics, one obtains

$$\delta h_{lm} = \frac{R}{4\pi c} \Gamma_{lm}^{l_1 l_2 m_1 m_2}(\Omega) H_{l_1 l_2 m_1 m_2}(T_0, T_F), \quad (15)$$

where  $l$  and  $m$  designate a spherical harmonic mode for each binary component,  $\delta h_{lm}$  is the overall non-linear memory for a given mode,  $R$  is the distance to the source,  $\Gamma_{lm}^{l_1 l_2 m_1 m_2}(\Omega)$  encodes the angular dependence of the memory as a function of radiation direction angles,  $\Omega$ , relative to the source, and  $H_{l_1 l_2 m_1 m_2}(T_0, T_F)$  encodes the memory's growth over the duration of the signal (Figure 7) (also  $H \propto 1/R^2$ , thus making  $\delta h_{lm}$  proportional to  $1/R$  like the oscillatory component).  $\Gamma_{lm}^{l_1 l_2 m_1 m_2}(\Omega)$  is a geometry factor closely related to the spherical harmonics and independent of the oscillatory waveform, and may thus, in part, be tabulated and inserted in advance before any waveform-specific calculations are made.  $H_{l_1 l_2 m_1 m_2}(T_0, T_F)$  is closely related to the total intensity of the secondary waveforms and thus must be computed after each signal is collected and processed. Using Equation (15), a tabulation of the spherical harmonics, and a properly chosen region of interest in an incident signal, the general relativity-

predicted nonlinear memory may be calculated as is done in Talbot *et al* [19].

A simple estimate of the memory suggested by Garfinkle [20] is given here. Consider two freely falling test masses separated by a distance  $r$ . An inverse relationship between the non-linear memory strain and  $r$  suggests a form for memory,  $\Delta h_b^a$ , given by Equation (16)

$$\Delta h_b^a = -\frac{m_b^a}{r}, \quad (16)$$

where  $m_b^a$  denotes the memory tensor. It can be shown that the memory tensor is related to the total radiated energy,  $E$ , and emission direction  $(\hat{\theta}, \hat{\phi})$  according to Equation (17)

$$m_b^a = -\frac{5}{14c^2} E \sin^2 \theta (\theta^a \theta_b - \phi^a \phi_b). \quad (17)$$

Combining Equations (16) and (17), we have

$$\Delta h_b^a = -\frac{5}{14c^2} \frac{E}{r} \sin^2 \theta (\theta^a \theta_b - \phi^a \phi_b), \quad (18)$$

or, in scalar form,

$$\Delta h = -\frac{5}{14c^2} \frac{E}{r} \sin^2 \theta. \quad (19)$$

Applying this result to GW150914 ( $E = 3.0 M_\odot \cdot c^2$ ,  $r = 410$  Mpc, and  $\theta = 150^\circ$ ), we find  $\Delta h \approx 3.0 \times 10^{-23}$ , which is roughly 3% of the oscillatory waveform's maximum amplitude.

Accurate identification and measurement of nonlinear memory will serve as a powerful test of general relativity. With the recent conclusion of the third LIGO observing run, much data are now available, allowing for the detectability of non-linear memory to be determined. From such a determination, the magnitude and nature of sensitivity improvements for each detector may be evaluated so non-linear memory can be effectively detected in future observing runs.

### D. Bayesian Parameter Estimation

In order to quantify our ability to detect and measure gravitational wave memory, we make use of standard techniques in Bayesian inferencing, as described in the following discussion.

Let the hypothesis  $H$  be the statement, "non-linear memory is present in the detector's data" and, further, let  $D$  be the detector's data. Then,  $P(H | D)$  is the probability that nonlinear memory is present in the data given the data we have at hand,  $P(D | H)$  is the likelihood that we will detect nonlinear memory given that nonlinear memory is, in fact, present,  $P(H)$  is the belief we have in the presence of nonlinear memory on the basis of prior information (or lack of information) alone, and  $P(D)$  is the evidence offered by the data independent of

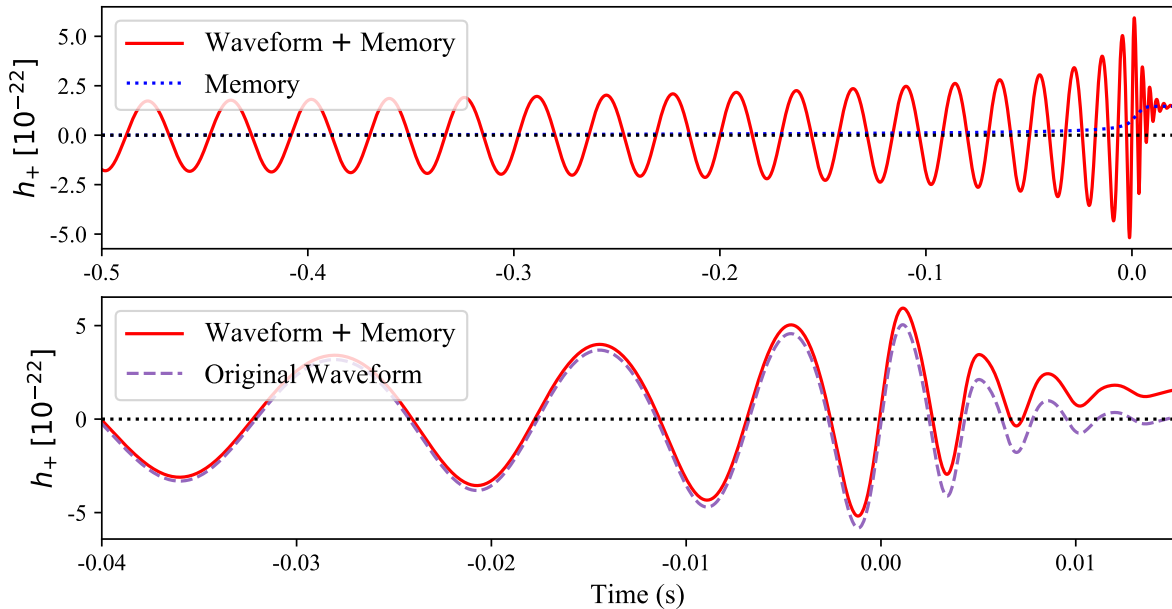


Figure 6. An example of a plus-polarized gravitational waveform with memory. The waveform approximant used is NRSur7dq2 and the source parameters include a total mass of  $60M_{\odot}$ , mass ratio of 2, and 0 spin for both components. (TOP) Inclusion of early inspiraling shows that most memory accumulates during the merger phase. (BOTTOM) Excluded inspiral stage with superposed waveforms, with and without memory, to illustrate the memory effect on waveforms.

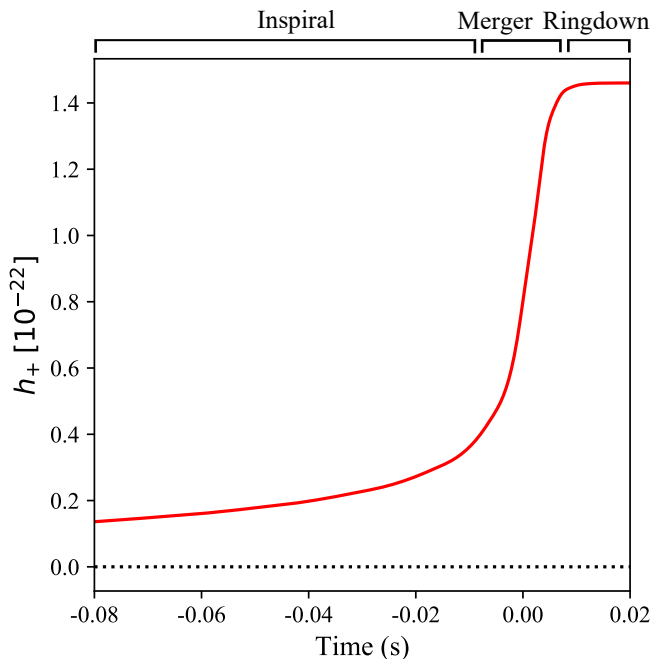


Figure 7. Time domain memory generated using the approximant NRSur7dq2, nonspinning components, a total mass of  $60M_{\odot}$ , and a mass ratio of 1.

the hypothesis under consideration. Bayes' Theorem relates these four quantities as shown in Equation (20).

$$P(H | D) = \frac{P(D | H) \times P(H)}{P(D)} \quad (20)$$

Equation (20) is used in Bayesian inferencing to update  $P(H | D)$  as more data becomes available, and we would like to satisfy Equation (20) by determining  $P(H | D)$  and  $P(\sim H | D)$  and computing the associated posterior odds. This process may be used to estimate pre-known parameter values and reasonable, or even improved, estimations with memory included in the model indicates a high likelihood of memory detectability.

However, in parameter estimation we would like to know how much memory is present. The first step is to present  $H$  as in Equation (21)

$$h_{\text{tot}} = h + \lambda h_{\text{mem}}, \quad (21)$$

where  $h_{\text{tot}}$  is the total signal,  $h$  is the non-memory portion of the signal, and  $h_{\text{mem}}$  is nonlinear memory. Then, for the injected template with known memory,  $\lambda = 1$  but for the purposes of parameter estimation can take on any value. A posterior distribution for  $\lambda$ , given in Equation (22), consistent with a value of 1 indicates a high likelihood of memory detection

Table I. Meanings for key symbols found in this section

Symbol	Meaning
$M_{\text{tot}}$	Total Mass
$q$	Mass Ratio ( $m_2/m_1$ )
$d_L$	Luminosity Distance
$\psi$	Polarization Angle
$\phi_c$	Coalescence Phase
$i$	Inclination Angle
$\alpha$	Right Ascension
$\delta$	Declination

$$P(\lambda | D, H) = \frac{P(D | \lambda, H) \times P(\lambda)}{P(D)}. \quad (22)$$

### III. PROCEDURE

In this project, we assess the detectability of memory in gravitational waves and subsequently search for methods to improve it. To achieve this goal, sufficient mastery of Bayesian parameter estimation, signal simulation, and python coding is needed. Here we will discuss the stages of this mastery, early experiments, experiments involving a bimodal distribution for  $\lambda$ , and a real-data experiment using GW150914. A legend for key symbols used throughout this section is given in Table I.

#### A. Summary and Preliminary Work

I will first begin with a brief outline of the project thus far.

(i) I first became familiar with python and PyCBC [21], a python package containing algorithms that can detect coalescing compact binaries and measure gravitational wave parameters. Garnering general python competency equipped me with the required coding skills that I used throughout the project, and PyCBC acquainted me with the general shape of gravitational waveforms and how to generate them.

(ii) I then became familiar with the python package GWmemory [19], which calculates and constructs nonlinear memory waveforms from selected gravitational signals. Gaining familiarity with this package improved my understanding of memory effects on gravitational wave signals and memory-laden waveform generation.

(iii) Directly afterward, I acquired a better understanding of Bayesian inference and became familiar with BILBY [22], a python package which consists of inferencing tools for parameter estimation.

(iv) At this point, I was well equipped to begin work on our primary goal. Equation (21) presents an all-or-nothing

waveform model for templates, where  $\lambda$  represents the memory constant. From the beginning, we planned to superpose a signal with memory (i.e.  $\lambda = 1$ ) on a typical noise distribution, and then apply matched filtering to measure the signal and infer the value of the memory constant. This inferred value would then represent the memory detectability, and a value close to 1 would mean that we are likely able to identify memory in a given signal. An outline of our process is given in Figure (8). Relevant experiments ensued.

(v) Following various experiments with simulated data, we then applied our approach to real data.

I will now discuss, in greater detail, points (i) - (iii) and cover points (iv) and (v) in the next two sections.

I attended SURF lectures on gravitational wave theory, noise and signal patterns, Bayesian inferencing, and detector geometry. I also completed theory and programming tutorials, which covered simulation of gravitational waves in the time and frequency domains. Transformation of signals between the time and frequency domains and worked examples of the matched filtering process were also included. Texts on Bayesian inferencing and practice with parameter estimation using various models, prior restrictions, and samplers improved my application ability and understanding of Bayes' rule. Because I used PyCBC and BILBY to complete many of these tutorials, I also acquired familiarity with these programs. Figures (1) and (4) show noise curves and a time-domain waveform that I generated during this time.

Multi-parameter estimation takes a long time to execute and, thus, preparations were made to work on the LIGO computing cluster. I began by installing a Linux virtual machine on my personal computer with python fully configured. BILBY, PyCBC, and GWmemory were then downloaded and installed. From here on, programs were written using VIM [23] to transition easily to the computing cluster later in the project. I then made frequency- and time-domain plots with GWmemory, familiarizing myself with memory waveforms. Several of these plots are given in Figures (6), (7), and (9).

Before moving into the Bayesian approach to parameter estimation, I began with a frequentist approach which handles 1- and 2-dimensional parameter estimation more efficiently than the Bayesian approach, but is not well optimized for higher-dimensional parameter spaces and disregards preexisting beliefs regarding the data's probability distribution function (PDF) because priors are nonexistent. In the frequentist approach, the location in parameter space for which a statistical index,  $\chi^2$ , is at a minimum marks the most likely values for each inferred parameter. The link between  $\chi^2$  and Gaussian likelihood is given in Equation (23)

$$\begin{aligned} & \log(P(D_i, f_i | \lambda, H)) \\ &= -\frac{1}{2} \left[ \sum_{i=1}^n \left( \frac{|D_i - (h_i + \lambda h_{\text{mem}})|^2}{\sigma_i^2} + 2\log(2\pi\sigma_i^2) \right) \right], \quad (23) \end{aligned}$$

where  $P(D_i, f_i | \lambda, H)$  is the likelihood associated with the data,  $D_i$ , and frequencies,  $f_i$ , given  $\lambda$  and the hypothesis,  $H$ ,

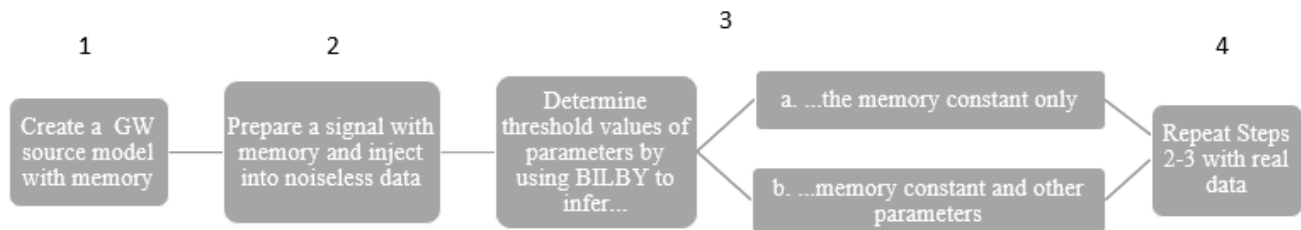


Figure 8. Flow chart which outlines our inferring process.

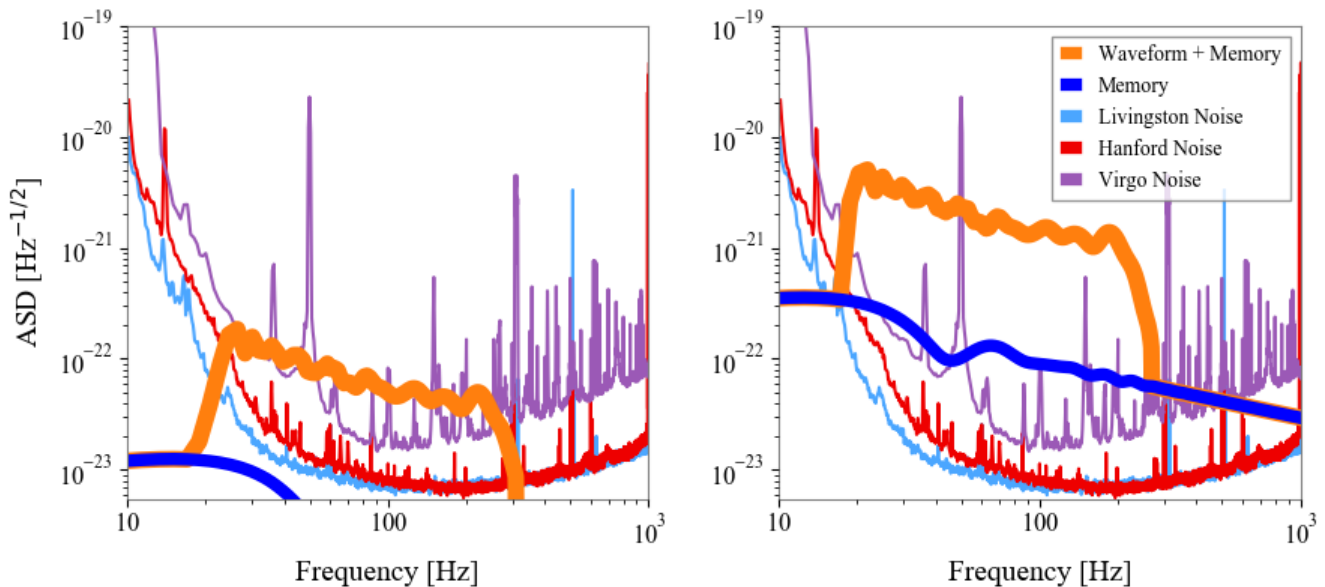


Figure 9. Waveforms in the frequency domain superposed with noise curves from the second observing run. It should be noted that the oscillatory waveform is generated from 20-Hz upward and is thus incorrect below this frequency. Since the memory contributed by a 20-Hz signal exists at far lower frequencies, the memory is correct over each of these plot’s domain, and clearly shows dominant power at sub-20-Hz frequencies. (LEFT) Source parameters are those of GW150914. Here, the predicted nonlinear memory (blue) cannot be detected in the data. (RIGHT) Both components are nonspinning with  $M_{\text{tot}} = 80M_{\odot}$ ,  $q = 1$ , and  $d_L = 20\text{Mpc}$ . If a signal sourced from a system with these parameters were incident on the detectors, the accompanying memory would likely be detectable.

that memory exists in the signal.  $\chi^2$  is the summation term on the right hand side of the equation. Clearly, if the goal is to find the location in parameter space for which  $\chi^2$  is at a minimum, then we could accomplish this goal by finding the location at which the likelihood is at a maximum. Figures (10) and (11) illustrate this approach graphically and analytically.

### B. Early Experiments

Following preliminary work, we completed a rudimentary version of our BILBY parameter estimation code which features a gravitational wave model with memory and uniform priors for all inferred parameters. At first, we only examined simulated data with high SNR ( $\approx 1000$ ) to debug the code, run simple experiments, and observe output effects when settings are varied. Figures (12) - (15) show sample corner plots for 1-, 2-, and 3-dimensional parameter estimation. In all cases, the high SNR allows for accurate parameter estimation, yet

the low-level noise still allows for differences in standard deviation between posterior distributions when, say, distance is varied. In all 1-dimensional probability distribution functions (PDFs), the orange vertical line demarcates the given parameter’s actual (simulated) value and the dotted, blue, vertical lines subtend the  $1\sigma$  confidence interval. In all 2-dimensional contour plots, the three regions in order of decreasing brightness are the  $1\sigma$ ,  $2\sigma$ , and  $3\sigma$  regions. Median values for the distributions are given above each inset plot.

### C. Lambda Bimodality Experiments

Lasky *et al* [24] predicts that a double degeneracy exists for the (2, 2) mode in polarization angle,  $\psi$ , and coalescence phase,  $\phi_c$ , leading to a bimodal distribution for  $\lambda$ . This bimodality arises because a (2, 2)-only oscillatory waveform with parameters  $(\psi, \phi_c)$  is unchanged by the transformation  $(\psi + 2\pi, \phi_c + 2\pi)$ , but, under the same transformation, the

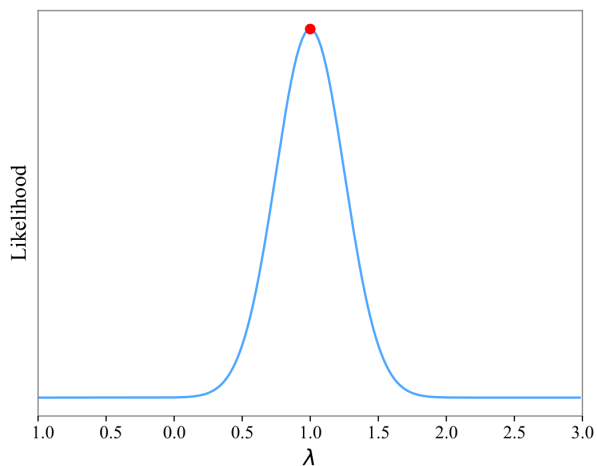


Figure 10. Plot of  $P(D|\lambda)$  vs.  $\lambda$  obtained by raising 10 to the power given in Equation (23). The injected waveform used to generate this likelihood distribution is sourced by non-spinning components with  $M_{\text{tot}} = 60M_{\odot}$ ,  $q = 1$ ,  $d_L = 100$  Mpc,  $\iota = \pi/2$ ,  $\psi = 0$ ,  $\phi_c = 0$ ,  $\alpha = 0$ ,  $\delta = 0$ . The red dot is the peak value and location computed through `scipy.optimize`.

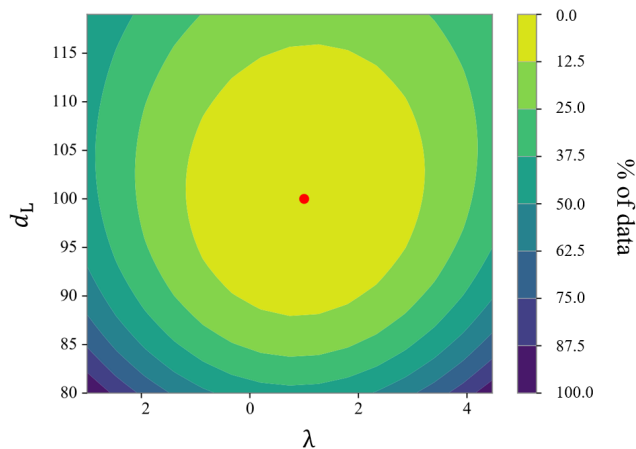


Figure 11. The injected waveform used to generate this likelihood distribution is sourced by non-spinning components with  $M_{\text{tot}} = 60M_{\odot}$ ,  $q = 1$ ,  $d_L = 100$  Mpc,  $\iota = \pi/2$ ,  $\psi = 0$ ,  $\phi_c = 0$ ,  $\alpha = 0$ ,  $\delta = 0$ . The red dot is the peak value and location computed through `scipy.optimize`.

memory constant changes sign. Including higher order modes breaks this degeneracy. Using Bayesian parameter estimation, we empirically prove this effect as shown in Figure (16).

Next, we found the distance at which the bimodality of  $\lambda$ 's PDF can be resolved and noted an interesting phenomenon which arises at  $d_L = 735$  Mpc when all modes are included. These observations, a discussion of this interesting feature, and the accompanying plots are all given in Figure (17).

From here, we also inferred the source's inclination angle,  $\iota$ . Working with only the (2, 2) mode, we compared noiseless and noisy data and found an, as yet, unexplained feature. The relevant plots and a discussion of this feature are given in

Figure (18).

Finally, we added in all modes and examined the results for noisy data at various distances. Corner plots for two distances and the accompanying observations are given in Figure (19).

#### D. GW150914

Finally, we applied our approach to GW150914 and found that  $\lambda = -0.65 \pm 2.25$ , which does not exclude zero. Thus, LIGO cannot detect memory for this event. The corner plot is given in Figure (20).

## IV. CONCLUSION

To determine the detectability of memory across the LIGO-VIRGO network, we built a model  $h_{\text{tot}} = h_{\text{osc}} + \lambda h_{\text{mem}}$ , designating  $\lambda$  as the memory constant. We then used Bayesian parameter estimation to infer  $\lambda$  from simulated and real data over various SNR values. After completing several simple experiments involving simulated, noiseless data, we confirmed the prediction by Lasky *et al* that  $\lambda$  switches parity under the transformation ( $\psi \rightarrow \psi + \pi/2$ ,  $\phi \rightarrow \phi + \pi/2$ ) only when higher-order modes are absent. We conclude that, in such cases,  $\lambda$  should be defined as positive, and the associated prior interval for  $\lambda$  should be bound on the left by 0. Finally, we applied our approach to GW150914 and found that memory is not detectable for this event.

From here, we would like to make the NRSur7dq4 approximant compatible with GWMemory, which will allow us to extend the upper mass ratio limit from 2 to 4, which is becoming more important as higher mass ratio binaries are being discovered [25]. We would also like to apply our approach to the remaining O1 and O2 events, and, later, all O3 events. Among these events, many promising candidates for memory detectability still remain. Even for GW150914, we can still improve analysis by using the method suggested in Hubner *et al* [26]. In short, we would use all of GW150914's memoryless posterior samples in our approach, averaging the final results to obtain a final posterior for  $\lambda$ . Our code has been improved greatly since its inception and is now able to handle a wider variety of source parameters. Also, average runtimes have been reduced by nearly 90%. However, further optimization in utility and efficiency is still worth investigating.

In the future, we wish to investigate a technique called event stacking which may allow us to detect memory for events with currently non-detectable memory. Using this technique, we would combine multiple, similar merger events, increasing  $\lambda$  and, thus, the statistical precision with which we can measure  $\lambda$ . How many events and how similar they must be for the method to be successful is a matter for further investigation, and will likely require the use of our approach in this project to answer.

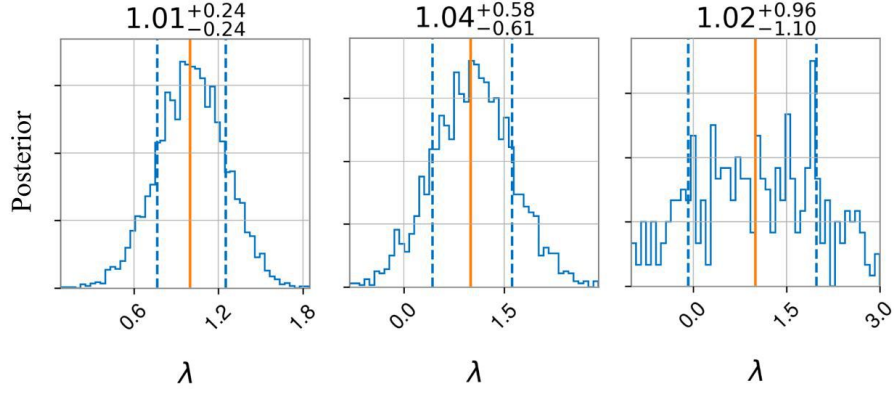


Figure 12. Standard deviation increases with distance, indicating that the data gives diminishing information for how to correct the prior. The injected waveform used to generate each plot is sourced by non-spinning components with  $M_{\text{tot}} = 60M_{\odot}$ ,  $q = 1.5$ ,  $\iota = \pi/2$ ,  $\psi = 0$ ,  $\phi_c = 0$ ,  $\alpha = 0$ ,  $\delta = 0$ . (Left)  $d_L = 100$  Mpc, (Center)  $d_L = 500$  Mpc, and (Right)  $d_L = 1000$  Mpc.

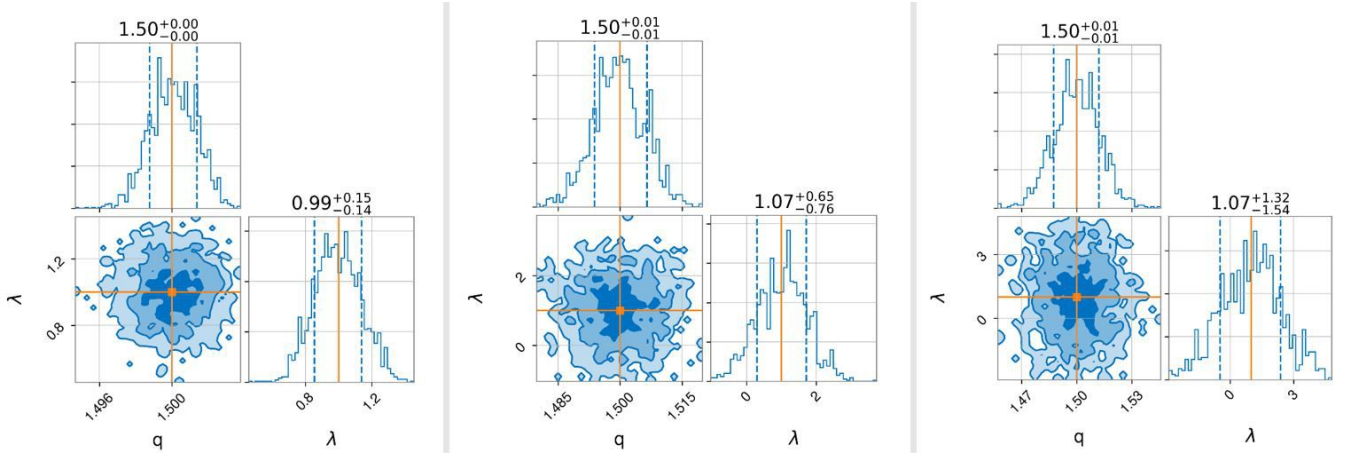


Figure 13. Both  $q$  and  $\lambda$ 's PDF widen with distance. The scales indicate that, unsurprisingly,  $q$  is measured more accurately than  $\lambda$  at each distance. The injected waveform used to generate each plot is sourced by non-spinning components with  $M_{\text{tot}} = 60M_{\odot}$ ,  $q = 1.5$ ,  $\iota = \pi/2$ ,  $\psi = 0$ ,  $\phi_c = 0$ ,  $\alpha = 0$ ,  $\delta = 0$ . (Left)  $d_L = 100$  Mpc, (Center)  $d_L = 500$  Mpc, and (Right)  $d_L = 1000$  Mpc.

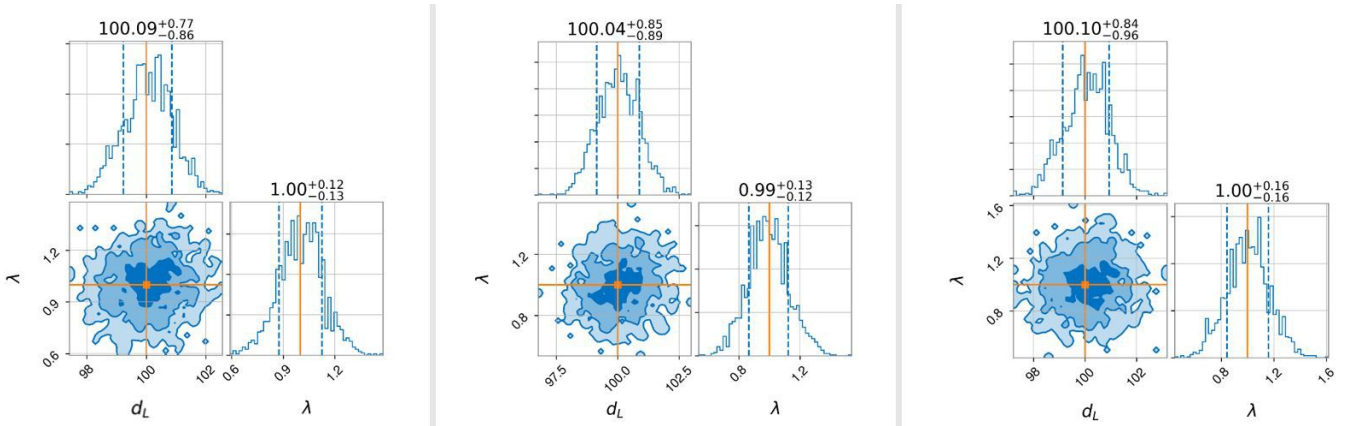


Figure 14. The posterior for  $d_L$  remains unchanged for each  $q$  value, but  $\lambda$ 's posterior increases in width for increasing  $q$ . The injected waveform used to generate each plot is sourced by non-spinning components with  $M_{\text{tot}} = 60M_{\odot}$ ,  $d_L = 100$  Mpc,  $\iota = \pi/2$ ,  $\psi = 0$ ,  $\phi_c = 0$ ,  $\alpha = 0$ ,  $\delta = 0$ . (Left)  $q = 1$ , (Center)  $q = 1.5$ , and (Right)  $q = 2$ .

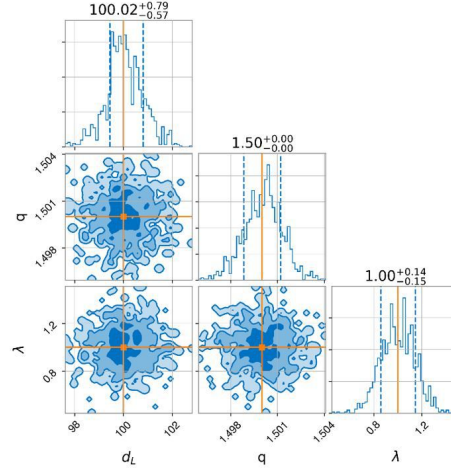


Figure 15. 3-dimensional parameter estimation for  $d_L$ ,  $q$ , and  $\lambda$ . The injected waveform used to generate each plot is sourced by non-spinning components with  $M_{\text{tot}} = 60M_{\odot}$ ,  $q = 1.5$ ,  $d_L = 100$  Mpc,  $\iota = \pi/2$ ,  $\psi = 0$ ,  $\phi_c = 0$ ,  $\alpha = 0$ ,  $\delta = 0$ .

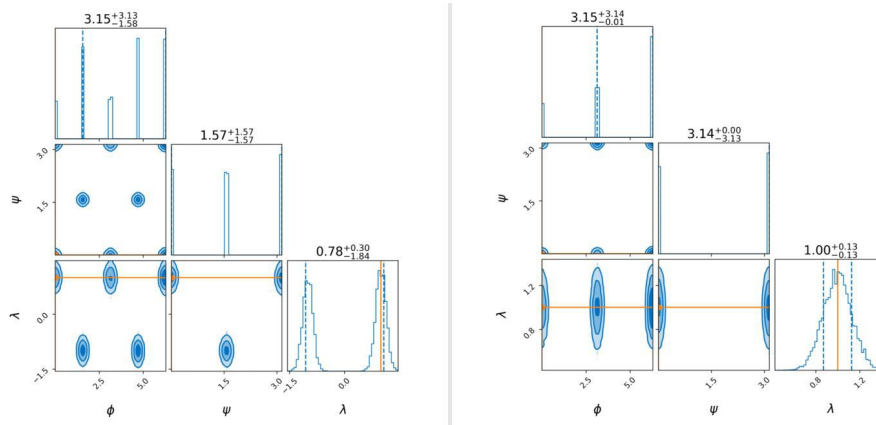


Figure 16. (Left) Inferring  $\psi$ ,  $\phi_c$ , and  $\lambda$  for a (2, 2) mode-only injected signal introduces bimodality in  $\lambda$ 's PDF. (Right) The bimodality is absent when higher order modes are introduced. The injected waveform used to generate each plot is sourced by non-spinning components with  $M_{\text{tot}} = 60M_{\odot}$ ,  $q = 1$ ,  $d_L = 100$  Mpc,  $\iota = \pi/2$ ,  $\psi = 0$ ,  $\phi_c = 0$ ,  $\alpha = 0$ ,  $\delta = 0$ .

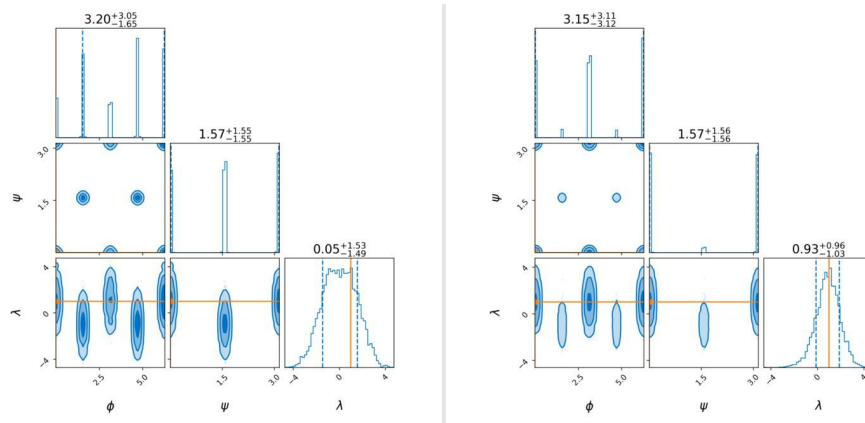


Figure 17. (Left) The distance is increased such that the (2, 2) mode-only peaks are non-resolvable. (Right) When higher order modes are added at this distance, an interesting phenomenon occurs:  $\psi$  and  $\phi_c$  become degenerate as the  $1\sigma$  line for  $\lambda$ 's PDF sweeps past  $\lambda = 0$ . At this point, non-trivial evidence is given for  $\lambda = -1$ , indicating (incorrectly) a bimodal distribution. The injected waveform used to generate each plot is sourced by non-spinning components with  $M_{\text{tot}} = 60M_{\odot}$ ,  $q = 1$ ,  $d_L = 735$  Mpc,  $\iota = \pi/2$ ,  $\psi = 0$ ,  $\phi_c = 0$ ,  $\alpha = 0$ ,  $\delta = 0$ .

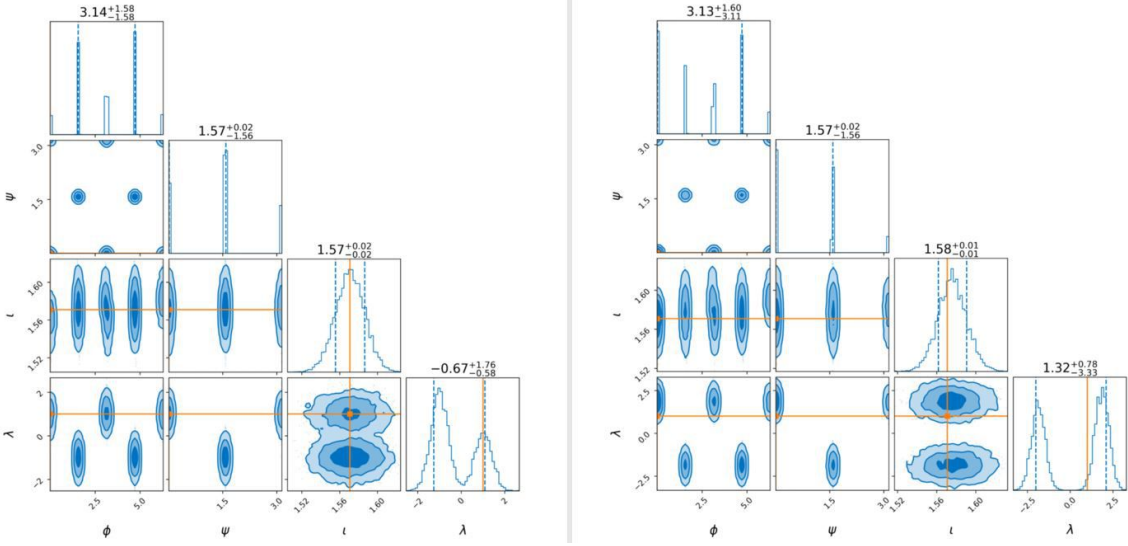


Figure 18. Both plots include (2, 2) mode-only waveform information and differ only in SNR. (*Left*) Noiseless data includes unequally-sized peaks in  $\lambda$ 's PDF. (*Right*) At this same distance, noisy data includes equally-sized peaks. The unequal peaks suggest greater evidence for negative memory in disagreement with Lasky *et al*'s prediction. This effect is present in every posterior sample of this kind generated, so sampling error is unlikely. At present, we are unable to explain why this effect occurs. The injected waveform used to generate each plot is sourced by non-spinning components with  $M_{\text{tot}} = 60M_{\odot}$ ,  $q = 1$ ,  $d_L = 280$  Mpc,  $\iota = \pi/2$ ,  $\psi = 0$ ,  $\phi_c = 0$ ,  $\alpha = 0$ ,  $\delta = 0$ .

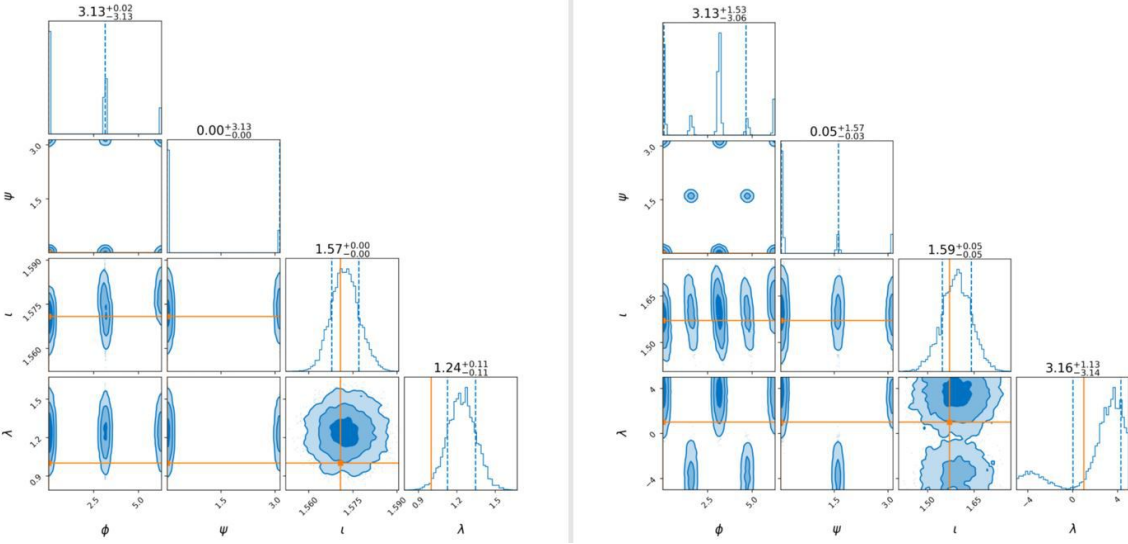


Figure 19. Plots include noisy, all-mode waveform information. (*Left*)  $d_L = 280$  Mpc. (*Right*) Increasing  $d_L$  to 950 Mpc causes the formation of a second peak in  $\lambda$ 's PDF for  $\lambda < 0$  and thus introduces degeneracy in  $\psi$  and  $\phi_c$ . The original peak has also shifted rightward, indicating that BILBY is unable to completely distinguish the waveform from the noise. The injected waveform used to generate each plot is sourced by non-spinning components with  $M_{\text{tot}} = 60M_{\odot}$ ,  $q = 1$ ,  $\iota = \pi/2$ ,  $\psi = 0$ ,  $\phi_c = 0$ ,  $\alpha = 0$ ,  $\delta = 0$ .

## V. ACKNOWLEDGMENTS

I thank my mentors Dr. Alan Weinstein, Dr. Colm Talbot, and Alvin K. Y. Li for their support and insight over the summer. I thank my teammates in the analysis group for input on my project. I thank Caltech LIGO SURF and LIGO Laboratory for organizing this research program and providing space for my project on the computing cluster. This research has made use of data obtained from the Gravitational Wave

Open Science Center (<https://www.gw-openscience.org>), a service of LIGO Laboratory, the LIGO Scientific Collaboration and the Virgo Collaboration. LIGO is funded by the U.S. National Science Foundation (NSF). Virgo is funded by the French Centre National de Recherche Scientifique (CNRS), the Italian Istituto Nazionale della Fisica Nucleare (INFN) and the Dutch Nikhef, with contributions by Polish and Hungarian institutes. This research was supported by the NSF REU program.

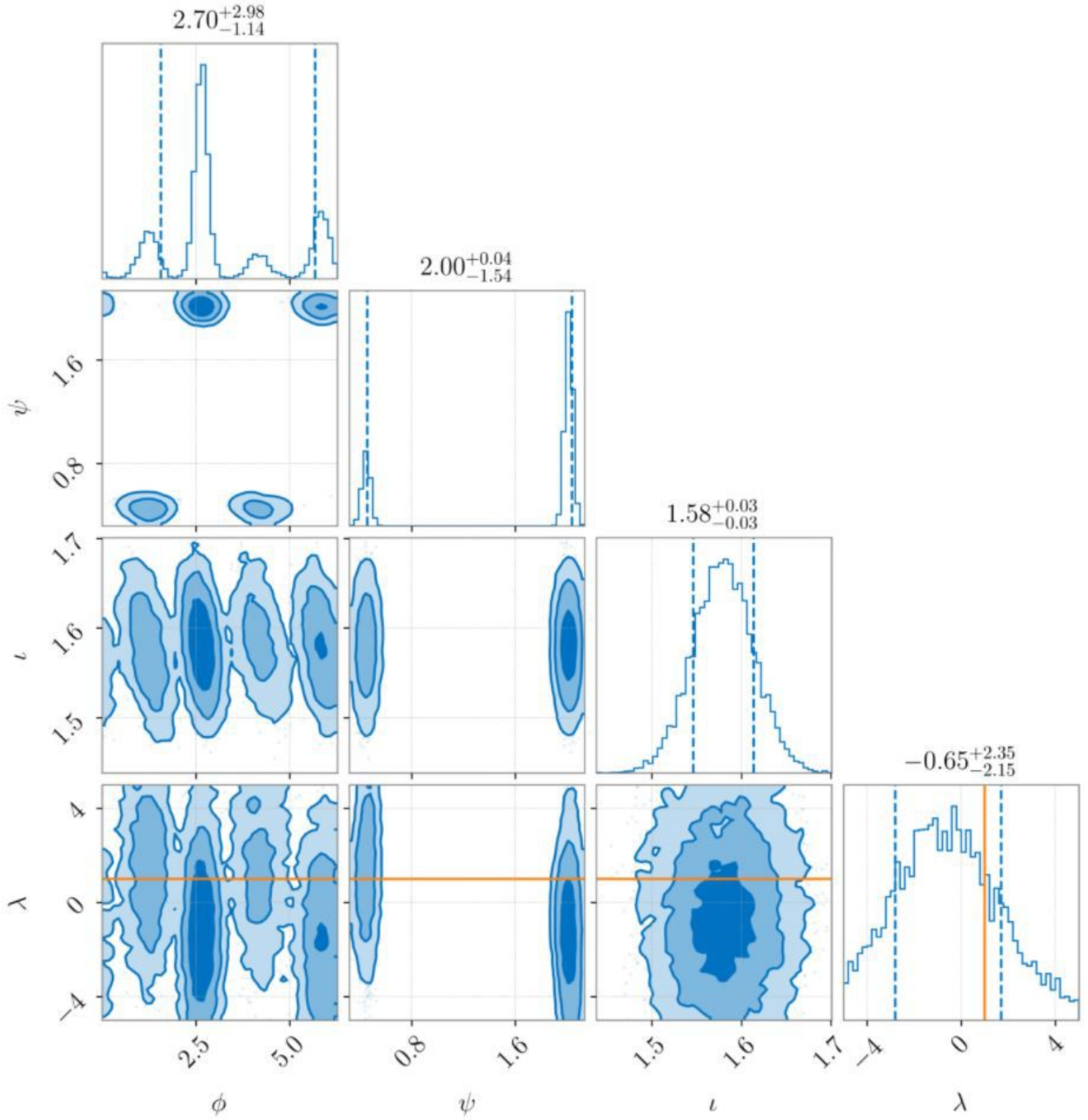


Figure 20. Strain data comes from GW150914. Non-inferred priors were retrieved from posterior samples obtained by memory-less parameter estimation. These values correspond to the maximum likelihood and are  $M = 70.4 M_{\odot}$ ,  $q = 1.1$ ,  $d_L = 342.2$  Mpc,  $\tau = 2.5$ ,  $\psi = 0$ ,  $\phi_c = 0$ ,  $\alpha = \delta = 1.2$ . As seen, memory cannot be detected for this event. Parameter values are retrieved from Abbott et al. [4].

- 
- [1] F. Pretorius. Evolution of binary black hole spacetimes. *Phys. Rev. Lett.*, 95(121101), 2005.
- [2] M. Campanelli et al. Accurate evolutions of orbiting black-hole binaries without excision. *Phys. Rev. Lett.*, 96(111101), 2006.
- [3] J. G. Baker et al. Gravitational-wave extraction from an inspiraling configuration of merging black holes. *Phys. Rev. Lett.*, 96(11), 2006.
- [4] B. P. Abbott et al. GWTC-1: A gravitational-wave transient catalog of compact binary mergers observed by LIGO and Virgo during the first and second observing runs. *Phys. Rev. X*, 9(3), 2019.
- [5] Y. B. Zeldovich and A. G. Polnarev. Radiation of gravitational waves by a cluster of superdense stars. *Sov. Astron.*, 18(17), 1974.
- [6] V. B. Braginsky and L. P. Grishchuk. Kinematic resonance and the memory effect in free mass gravitational antennas. *Sov. Phys. JETP*, 62(3):427–430, 1985.
- [7] V. B. Braginsky and K. S. Thorne. Gravitational-wave bursts with memory and experimental prospects. *Nature*, 327(6118): 123–125, 1987.
- [8] Kip S. Thorne. Gravitational-wave bursts with memory: The christodoulou effect. *Phys. Rev. D*, 45(2):520–524, 1992.
- [9] M. Favata. The gravitational-wave memory effect. *Classical Quant. Grav.*, 27(8), 2010.
- [10] A. Einstein. On gravitational waves. *Sitzungsber. Preuss. Akad. Wiss.*, 1:135–149, 1918.
- [11] H. Velten, J. B. Jimenez, and F. Piazza. Limits on the anomalous speed of gravitational waves from binary pulsars. *Int. J. Mod. Phys. Conf. Ser.*, 45(1760016), 2017.
- [12] B. P. Abbott et al. Gravitational waves and gamma-rays from a binary neutron star merger: GW170817 and GRB 170817A. *ApJ*, 848(2):L13, 2017.
- [13] S. Klimentenko et al. Method for detection and reconstruction of gravitational wave transients with networks of advanced detectors. *Phys. Rev. D*, 93, 2016.
- [14] N. Christensen. Stochastic gravitational wave backgrounds. *Rept. Prog. Phys.*, 82(1), 2018.
- [15] M. A. Papa et al. Search for continuous gravitational waves from the central compact objects in supernova remnants Cassiopeia A, Vela Jr., and G347.3-0.5. *ApJ*, 897(1), 2020.
- [16] S. Mukherjee et al. Classification of glitch waveforms in gravitational wave detector characterization. *Phys. Conf. Ser.*, 243 (012006), 2010.
- [17] D. V. Martynov et al. Sensitivity of the advanced LIGO detectors at the beginning of gravitational wave astronomy. *Physical Review D*, 93(112004), 2016.
- [18] H. Gabbard et al. Matching matched filtering with deep networks in gravitational-wave astronomy. *Phys. Rev. Lett.*, 120, 2017.
- [19] C. Talbot et al. Gravitational-wave memory: waveforms and phenomenology. *Phys. Rev. D*, 98(6), 2018.
- [20] D. Garfinkle. A simple estimate of gravitational wave memory in binary black hole systems. *Classical Quant. Grav.*, 33(17), 2016.
- [21] C. M. Biwer et al. Pycbc inference: A python-based parameter estimation toolkit for compact binary coalescence signals. *PASP*, 131(996), 2019.
- [22] G. Ashton et al. Bilby: A user-friendly bayesian inference library for gravitational-wave astronomy. *Astrophys. J. Suppl. Ser.*, 27(241), 2019.
- [23] A. Kowarik and M. Templ. Imputation with the R package VIM. *J. Stat. Softw.*, 74(7):1–16, 2016.
- [24] P. D. Lasky et al. Detecting gravitational-wave memory with LIGO: Implications of GW150914. *Phys. Rev. Lett.*, 117, 2016.
- [25] R. Abbott et al. GW190814: Gravitational waves from the coalescence of a 23 solar mass black hole with a 2.6 solar mass compact object. *Astrophys. J. Lett.*, 896(2), 2020.
- [26] M. Hubner et al. Thanks for the memory: measuring gravitational-wave memory in the first LIGO/VIRGO gravitational-wave transient catalog. *Phys. Rev. D*, 101 (023011), 2020.